#### **RESEARCH ARTICLE**



# Secondary circulation within a mixing box and its effect on turbulence

Hadis Matinpour<sup>1</sup> · Joseph Atkinson<sup>1</sup> · Sean Bennett<sup>2</sup>

Received: 27 April 2020 / Revised: 18 September 2020 / Accepted: 21 September 2020 © Springer-Verlag GmbH Germany, part of Springer Nature 2020

#### **Abstract**

An experimental study was conducted to examine the formation of secondary circulation in a grid-mixing box and to determine its effect on turbulence. This apparatus has been used extensively to study turbulence and mixing in a variety of geophysical contexts, and it is commonly assumed that turbulence is nearly isotropic and horizontally homogenous and that it is a zero-mean shear flow. Exceptions to these assumptions, however, have been reported, where a secondary flow pattern has been observed consisting of two roughly symmetric large-scale circulations with upward flow in the center of the box and downward return flow along the sides. These secondary flows appear to be associated with different grid oscillation conditions and box and grid geometries, and criteria have been proposed to describe conditions when secondary flow may be expected. Experiments were conducted for three different combinations of the grid oscillation stroke and frequency, while maintaining a near constant grid Reynolds number, to examine the formation and strength of the secondary flow and its effect on the magnitude and distribution of turbulence within the box. Velocity characteristics were obtained by particle image velocimetry (PIV). Results show that (1) secondary circulations were present for all combinations of the grid oscillation conditions; (2) as stroke length increased, the intensity of the secondary circulation and the contribution of these motions to total kinetic energy increased; and (3) the presence of secondary circulation results in greater overall mixing and turbulent transport in the region close to the grid. These insights are expected to be relevant to a wide range of mixing box applications.

Published online: 10 October 2020



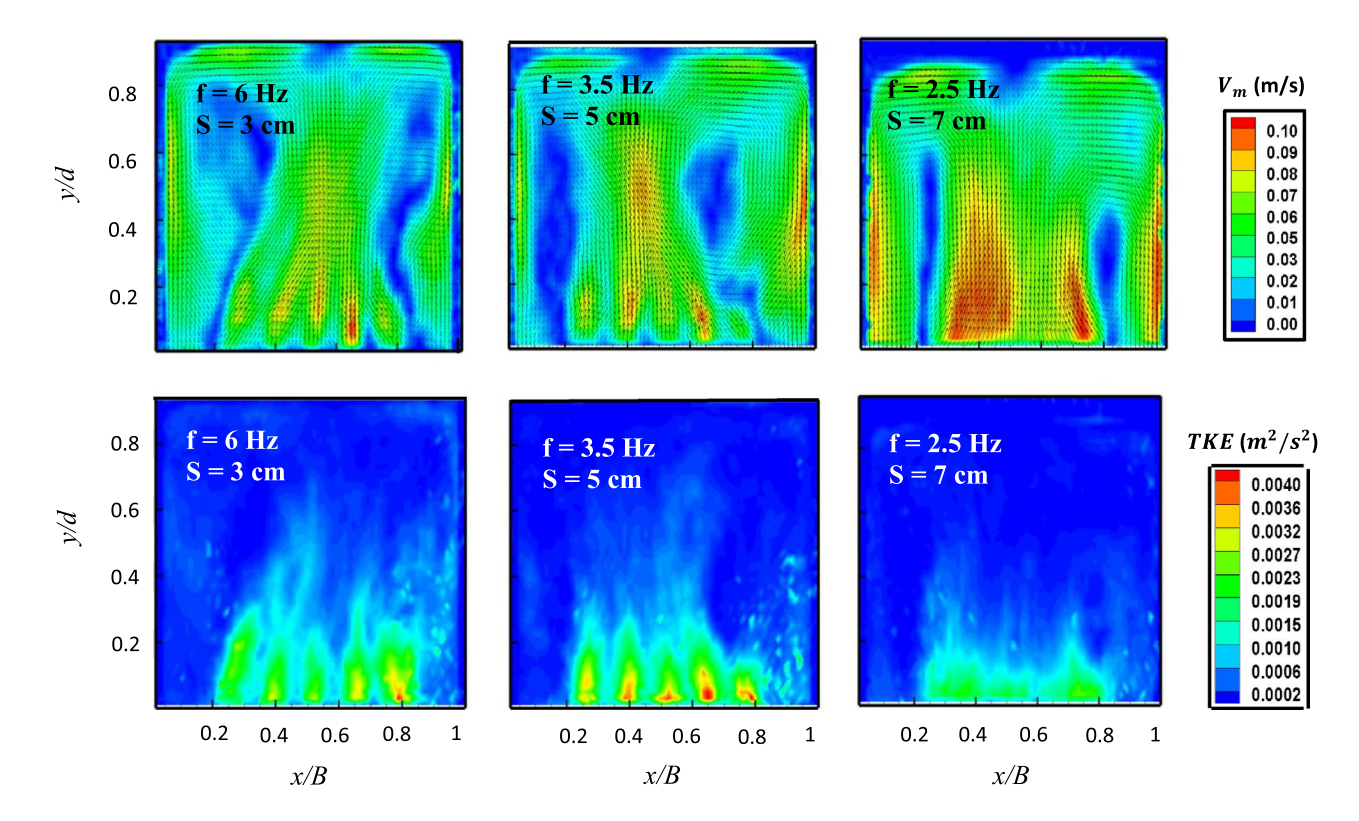
Hadis Matinpour hadismat@buffalo.edu

Department of Civil, Structural and Environmental Engineering, University at Buffalo, Buffalo, USA

Department of Geography, University at Buffalo, Buffalo, USA

225 Page 2 of 13 Experiments in Fluids (2020) 61:225

## **Graphic abstract**



# 1 Introduction and background

Turbulence and associated transport characteristics are important for many physical processes on the Earth's surface. A convenient means of studying turbulence in a laboratory setting is with a mixing box, or oscillating grid tank (OGT), which is a rectangular or cylindrical container with an oscillating grid that produces the mixing motion. In this setup, a planar grid of crossed bars oscillates in the direction normal to the grid (usually vertically) and produces a series of jets and wakes behind the grid bars that spread, interact with each other, and break down into turbulence (Thompson and Turner 1975; Hopfinger and Toly 1976).

OGTs have been used in a variety of applications. They were initially employed to study fluid mixing across a density interface (Thompson and Turner 1975; Hopfinger and Toly 1976; McDougall 1979; Hannoun et al. 1988; McGrath et al. 1997). De Silva and Fernando (1998) used an OGT to simulate turbulence patches and associated mixing in a linearly stratified fluid as found in oceans. The apparatus also has been used to study the physics of turbulence and its comparison to theory (De Silva and Fernando 1994; Villermaux et al. 1995; Matsunaga et al.

1999; Cheng and Law 2001; Janzen et al. 2003; Schulz et al. 2006; Wan Mohtar 2016). Huppert et al. (1995) used a mixing box to examine sediment entrainment in a dense suspension layer stirred by an oscillating grid. Mixing boxes were used to explore sediment suspension and the interactions between suspended sediment and turbulent flow (Bennett and Best 1995; Redondo et al. 2001; Orlins and Gulliver 2003; Belinsky et al. 2005; Bennett et al. 2014; Matinpour et al. 2019), while others have investigated sediment incipient motion (Medina et al. 2001; Liu et al. 2011; Rastello et al. 2020). In engineering applications, mixing boxes have been used to study the gas-fluid transfer process (Herlina and Jirka 2008) and bio-related turbulence such as the effect of submerged aquatic vegetation on turbulence (Pujol et al. 2012) and the effect of turbulence on plankton (Guadayol et al. 2009). The present study is part of a larger investigation that seeks to examine sediment-turbulence interactions, which requires the grid to be located near the bottom similar to Huppert et al. (1995), Bennett et al. (2014), and Matinpour et al. (2019). This grid placement is in contrast to many studies where the grid is located near the free surface or middle of the water column (see below).



Experiments in Fluids (2020) 61:225 Page 3 of 13 225

Thompson and Turner (1975) and Hopfinger and Toly (1976) showed that a vertically oscillating grid produces horizontally homogenous turbulence that decays with distance from the grid as

$$\left[u^{2}\right]^{0.5} = u_{\rm rms} = c_{1} M^{0.5} S^{1.5} f y^{*-1} \tag{1}$$

$$\left[v^{\prime 2}\right]^{0.5} = v_{\rm rms} = c_2 M^{0.5} S^{1.5} f y^{*-1} \tag{2}$$

$$\zeta = c_3 y^* \tag{3}$$

where u' and v' are horizontal and vertical turbulent fluctuation velocities (the brackets indicate time-averaged values), respectively,  $u_{\rm rms}$  and  $v_{\rm rms}$  are horizontal and vertical root-mean-square velocities, respectively, M is the center-tocenter mesh spacing of the grid, S is the stroke length, f is the grid oscillation frequency (Hz), y\* is distance from the grid center plane,  $\zeta$  is the integral turbulent length scale, and  $c_1$ ,  $c_2$ , and  $c_3$  are constants that depend on experimental configuration and the grid geometry. This representation of turbulence decay with height above the grid has been adopted in many studies (Hopfinger and Toly 1976; Fernando and De Silva 1993; De Silva and Fernando 1994; Cheng and Law 2001; Orlins and Gulliver 2003). A slight modification of these relationships was proposed by Atkinson et al. (1987), who showed that Eqs. 1 and 2 are applicable only for distances greater than about two mesh sizes away from the grid  $(y^* > 2 \text{ M})$ , which was experimentally confirmed elsewhere (De Silva and Fernando 1994; Orlins and Gulliver 2003).

Ideally, turbulence in a mixing box with an oscillating grid is isotropic, it is homogenous in planes parallel to the grid, and it decays with distance from the grid (De Silva and Fernando 1994). Most of the studies listed above assume that the physical processes in these boxes, such as interfacial mixing, sedimentation, and gas transfer, occur in the absence of a mean flow. Ideal conditions, however, are not always achieved, and it has been shown that oscillating grids can produce significant secondary circulation (Hopfinger and Toly 1976; Fernando and De Silva 1993; Dohan and Sutherland 2002; McKenna and McGillis 2004; Variano and Cowen 2008; Bennett et al. 2014). Even accepting that the energy of secondary circulation motions is less than 10% of the total fluid kinetic energy (Hopfinger and Toly 1976; McCorquodale and Munro 2017), these larger-scale motions will affect turbulent transport. In some cases, the strength of secondary circulation can be substantial, representing up to 25% of total kinetic energy (Dohan and Sutherland 2002; McKenna and McGillis 2004).

Several mechanistic causes for this secondary motion have been advanced. Fernando and De Silva (1993) considered different grid configurations (see below) and suggested that secondary mean flow is caused by weak spatial gradients in turbulent shear stress parallel to the grid. These gradients affect the grid-normal orientation and mixing of the jets formed by the oscillating grid, creating fewer, stronger jets that appear as secondary flow. Similarly, McCorquodale and Munro (2018) and Lacassagne et al. 2020; see Drayton, 1993, cited therein) proposed that the relative strength and the grid-normal orientation of the jets can be affected by a combination of grid-edge effects and side-wall effects, thus producing secondary circulation.

To obtain nearly isotropic zero-mean-shear flow in OGTs, the following criteria have been suggested: (1) S should be greater than 1 cm and less than or equal to M ( $S \le M$  or  $S/M \le 1$ ; Hopfinger and Toly 1976; McDougall 1979); (2) f should be less than 7 Hz (McDougall 1979); and (3) the grid solidity, defined as the ratio of projected area of the grid bars to cross sectional area of the box, should be less than 40% (Hopfinger and Toly 1976).

An additional consideration was shown by Fernando and De Silva (1993), who performed two series of experiments in an OGT where the only difference was the grid configuration. In the first series, the grid was made by crossed square bars without parallel grid bars close to the wall (Fig. 1a), and in the second series, the grid was made with parallel bars adjacent to the walls (Fig. 1b), but M, f, and S were kept constant with values of 0.0476 m, 4.5 Hz, and 0.021 m, respectively. While these conditions met the above criteria for achieving nearly isotropic zero-mean-shear flow, the grid in Fig. 1b, referred to as the grid with faulty end-condition, produced substantial secondary circulation. McCorquodale and Munro (2018) suggested installing an inner box, thus isolating the wall-induced jet distortions that produce the secondary flow from the main flow field.

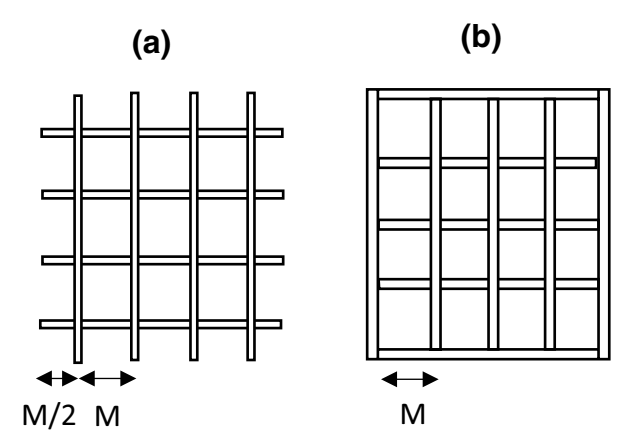


Fig. 1 Schematic drawing of a grid with **a** correct end conditions and **b** faulty end conditions (adapted from Fernando and De Silva 1993)



Dohan and Sutherland (2002) investigated turbulence time scales in a mixing box and found that for a high ratio of the total water depth D to the box internal width B, a mean circulation pattern develops. They observed a pair of large counter-rotating vortices in experiments when D > B, but when  $D/B \sim 1$ , the circulation cells were not observed. This result was explained as when the vertical length scale of the box is much greater than the horizontal length scale, the grid-generated flow structure changes from relatively smaller-scale, three-dimensional turbulence to relatively larger-scale, two-dimensional turbulence. In their experiment, grid solidity was 27% (less than 40%) and M, f, and S were 0.032 m, 7 Hz, and 0.026 m, respectively. While these conditions all agree with the above-stated criteria to avoid secondary circulation with f at its upper limit, this work suggests that D/B is another important parameter.

McKenna and McGillis (2004) performed tests in a mixing box with D/B = 1.26 and a correct end-condition grid with solidity less than 40% to study the existence of secondary circulation, and observed secondary circulation patterns with substantial mean flow representing up to 25% of the total kinetic energy. In their experiments M = 0.064 m, f < 2.25 Hz, and S varied between 0.064 m and 0.114 m. With S > 0.07 m and S/M > 1, secondary flows might be expected in these experiments using the above criteria, but it is not clear whether S (or S/M) or D/B was more directly related to this flow condition.

In summary, factors involved in formation of secondary circulation include grid oscillation conditions (f, S), the grid end condition, the ratio of depth to width of the box, and the grid solidity. There is, however, no clear consensus about formation of secondary circulation in OGTs and its influence on turbulent transport and mixing. In this study, the effects of the grid oscillation conditions on the formation and magnitude of secondary flow are examined, and the grid location near the bottom introduces an additional factor as discussed further below. All other boundary conditions were chosen to minimize the formation of secondary flow according to the above-listed criteria. The main objectives of this paper are: (1) to quantify the effects of the combination of S and f on the formation of secondary flow in an OGT with the grid located near the bottom; and (2) to examine the effects of secondary circulation on turbulence decay rate, transport, integral length-scales, and the degree of isotropy.

# 2 Experimental Design

The experiments were performed in the same mixing box used by Bennett et al. (2013, 2014) and Matinpour et al. (2019), which is nearly identical to the apparatus used by Bennett and Best (1995) and Huppert et al. (1995). In these tests the location of the grid was near the bottom because

of companion work focused on sediment suspension tests (Matinpour et al. 2019). This placement is in contrast to many studies in which the grid is located near the top or at the mid-horizontal-plane of the box (Thompson and Turner 1975; Hopfinger and Toly 1976; Atkinson et al. 1987; Hannoun et al. 1988; De Silva and Fernando 1994; Dohan and Sutherland 2002; Orlins and Gulliver 2003; McCorquodale and Munro 2017). In addition, a larger stroke was used relative to earlier studies, again motivated by the sediment-related tests.

The mixing box is a rectangular polycarbonate tank 0.01 m thick with internal dimensions of  $0.313 \times 0.313$  m (B = 0.313 m) in cross-section and 0.40 m high (Fig. 2). The aluminum grid consists of an intersecting  $5 \times 5$  mesh of square bars 0.295 m long and 0.01 m thick, with a mesh spacing M = 0.05 m and a grid solidity of 30%. The gap between the edge of the tank and the grid is 9 mm. The grid is attached to a 0.125-m diameter stainless steel bar with an eccentric connection to an external electrical motor to produce oscillation. For all values of S used, the lowest extent of the grid in its oscillation cycle is a few millimeters above the bottom of the tank. The box was filled with tap water to a height of 0.27 m (total water depth D) and D/B = 0.86.

Velocities were measured with two-dimensional particle image velocimetry (PIV). The PIV system consists of a dual cavity 50 mJ Nd-YAG laser emitting 532 nm light and one 4 Mp camera. Hollow glass spheres 25 µm in diameter were used as fluid tracer particles. To quantify the turbulence signals, 2400 paired images were captured over a 30-s period at 80 Hz. The time lapse between pulses was 2500 µs. An adaptive cross-correlation algorithm within the commercial software (DANTEC Dynamic Studio) was used to derive instantaneous velocities and vector maps based on the acquired paired images. Interrogation areas applied in the cross-correlation algorithm were 32 × 32 pixels. Spurious vectors were deleted and the results were obtained based on valid vectors only. The calibration image shows that each pixel corresponds to 0.138 mm and the size of the interrogation area was 4.4 × 4.4 mm. The spatial dimension of the field of view is  $0.32 \times 0.20$  m.

To investigate the impacts of S and f on the turbulent flow field, three experimental conditions were examined: (1) Run 1 where S = 0.03 m and f = 6 Hz; (2) Run 2 where S = 0.05 m and f = 3.5 Hz; and (3) Run 3 where S = 0.07 m and f = 2.5 Hz. These combinations were selected so that grid velocity was nearly constant and could be used as a basis for comparison. Data for each run presented here represent five repeated tests that were averaged at-a-point, in order to develop better assurance of data quality.

It is noted that only three combinations of f and S were selected due to the experimental limitations of the apparatus used. Specifically, we found that relatively very low or very high values of f and S were incapable of producing



Experiments in Fluids (2020) 61:225 Page 5 of 13 225

**Fig. 2** Schematic drawings of the **a** top and **b** side views of the mixing box set-up and PIV system

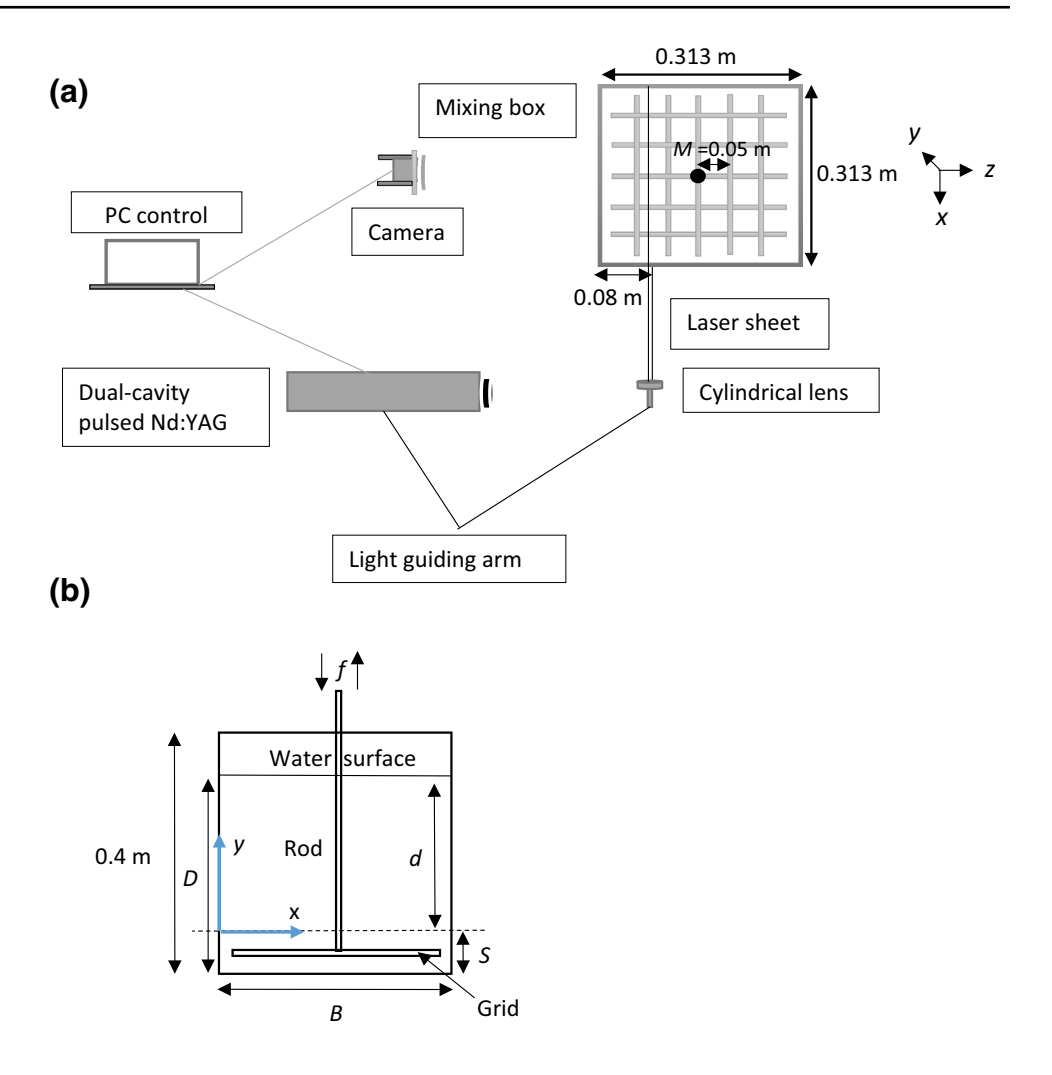


**Table 1** Conditions for each experimental run including S, f,  $Re_G$ , S/M, and fS

Combination number	Stroke length S (m)	Oscillation frequency $f$ (Hz)	$Re_G$	S/M	fS (m/s)
Run 1	0.03	6.0	9000	0.6	0.180
Run 2	0.05	3.5	8750	1.0	0.175
Run 3	0.07	2.5	8750	1.4	0.175

requisite flow fields within the current boundary conditions of the mixing box apparatus. Note that M = 0.05 m was constant for all three runs and S was selected to be two units less than M, equal to M, and two units greater than M to describe the effect of the relative size of S to M. The grid Reynolds number  $Re_G$ , defined by McCorquodale and Munro (2018) as

$$Re_{G} = MSf/v \tag{4}$$

where  $\nu$  is the kinematic viscosity of water, had values of 9000 for Run 1 and 8750 for Runs 2 and 3 (Table 1). For comparison, previous studies using OGTs used Re<sub>G</sub> between 500 and 8100 (McDougall 1979; Hannoun et al. 1988; Herlina and Jirka 2008; McCorquodale and Munro 2017).

In all experiments, a laser light sheet 1-mm thick was introduced parallel to the x-y plane 0.08 m from the sidewall (Fig. 2), where x is horizontal distance measured from the right wall of the box and y is vertical distance from the highest position of the grid (i.e.,  $y = y^* - S/2$ ). Data were recorded from x/B = 0.01 to 0.99 and from y/d = 0.02 to 0.98, where d is the flow depth measured from the highest position of the grid to the water surface (Fig. 2).

Because secondary circulation was previously observed using this apparatus (Bennett et al. 2014), preliminary experiments were conducted to understand the spatial variation of flow within the mixing box. Two-dimensional PIV measurements were obtained for seven parallel planes for z/B = 0.064, 0.128, 0.192, 0.256, 0.319, 0.383 and 0.447. In these preliminary tests, D = 0.27 m, S = 0.07 m, and f = 3 Hz, or fS = 0.21 m/s (Matinpour et al. 2015). These preliminary



experiments established that (1) the vertical variation of horizontally averaged two-dimensional turbulent kinetic energy  $\langle TKE \rangle$  (defined below) was reduced at distances z/B < 0.223, confirming a significant front-wall effect, and (2)  $\langle TKE \rangle$  was near its maximum value at a distance of about z/B = 0.256, and (3)  $\langle TKE \rangle$  decreased slightly at distances z/B > 0.256 m, toward the center of the box. On the basis of these preliminary observations, we selected the plane at z/B = 0.256 (or 0.08 m from the sidewall) for data collection, which is directly above the mid-point of the cross-bars of the grid (Fig. 2).

# 3 Analysis and results

### 3.1 Planar observations

Instantaneous flow velocities in x and y directions, u(x,y,t) and v(x,y,t) respectively, are quantified using aggregation of the PIV data for the five repeat experiments for each run,

$$u(x, y, t) = \frac{1}{5} \sum_{i=1}^{5} u_i(x, y, t)$$
 (5)

$$v(x, y, t) = \frac{1}{5} \sum_{i=1}^{5} v_i(x, y, t)$$
 (6)

Time-averaged flow velocities in x and y directions, u and v respectively, are defined using standard turbulence decomposition (also see Eqs. 1 and 2),

$$[u] = u - u' \tag{7}$$

$$[v] = v - v' \tag{8}$$

The magnitude of the mean velocity  $V_m$  is defined by

$$V_m = ([u]^2 + [v]^2)^{0.5}$$
(9)

To assess the repeatability of the flow conditions within the mixing box, error analysis was performed on five repeated tests. The average relative standard errors calculated for horizontal and vertical mean flow velocities at-a-point are 9% and 18%, respectively. This result is consistent with those reported by McKenna and McGillis (2004), who assessed flow repeatability in an OGT. It is noted that in experiments with nominally identical oscillation grid conditions, the influence of time-variability in mean flow velocities was observed, which may be unavoidable in using OGTs (McKenna and McGillis 2004). In the present tests the OGT data presented are likely unaffected by non-steady state flow conditions based on the following criteria: (1) the time-periods between OGT start-up

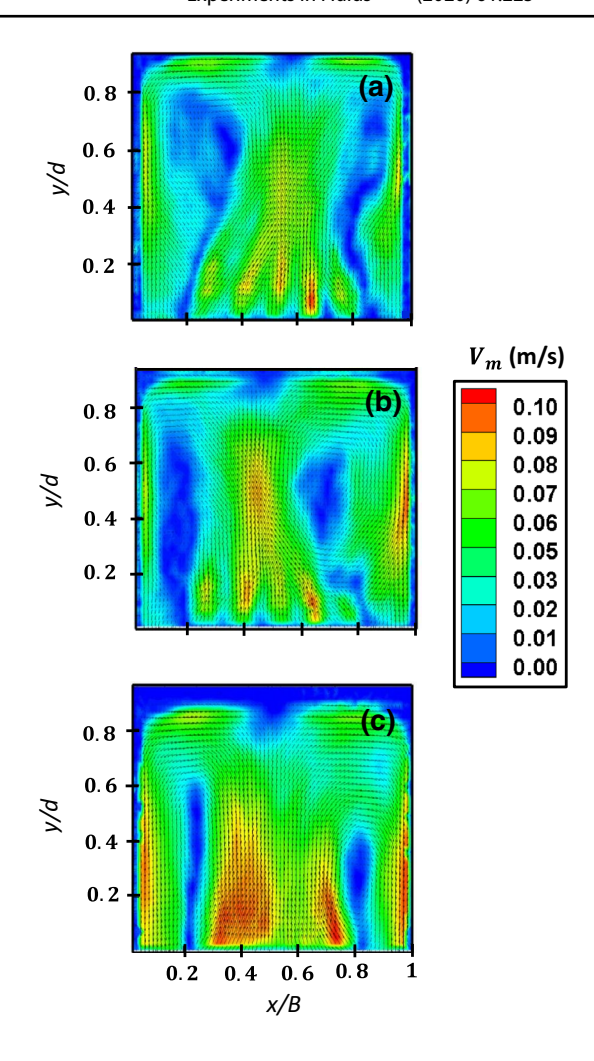


**Fig. 3** The magnitude of mean velocity contour maps along with vector maps for different combinations of S and f: **a** S=0.03 m and f=6 Hz for Run 1, **b** S=0.05 m and f=3.5 Hz for Run 2, and **c** S=0.07 m and f=2.5 Hz for Run 3

and data collection ranged from 20 to 25 min, (2) each run represents an average of five individual datasets taken over 6 h, and (3) analysis of selected TKE time-series showed that the slopes of linear regression lines were not statistically different from zero. The influence of time variability in mean flow is relatively small in comparison to the mean flow velocity differences observed between the experiments (see Figs. 3, 5a, d).

Figure 3 shows the planar distributions of  $V_m$  for the three runs with different combinations of S and f listed in Table 1. In all experiments,  $V_m$  is highest in the center of the box and close to the walls. Vector maps, also shown in Fig. 3, indicate that the time-averaged flow is upward in the center of the box and downward close to the walls. Regardless of the combination of S and f, a secondary circulation pattern is present. Figure 3 shows a progression toward relatively stronger secondary flow from Run 1 to 3, indicating the



Experiments in Fluids (2020) 61:225 Page 7 of 13 225

effect of larger stroke length on the intensity of secondary flow. For Run 3 with the largest S (S=0.07 m and f=2.5 Hz), the secondary flow appears to be better developed, and the maximum value of  $V_m$  ( $\approx$  0.1 m/s) is distributed over a much larger area of the flow field in comparison to Runs 1 and 2.

Turbulent kinetic energy TKE per unit mass at-a-point is defined by horizontal and vertical root-mean-square velocities,  $u_{rms}$  and  $v_{rms}$  (see Eqs. 1 and 2),

$$TKE = 0.5 \left( u_{rms}^2 + v_{rms}^2 \right) \tag{10}$$

Analysis performed on five repeated tests showed that the average relative standard error calculated at-a-point for TKE per unit mass is 8%. It is also noted that Eq. (10) defines two-dimensional TKE. This definition is used since the only available data were in the x and y directions (we did not invoke the similarity assumption that  $w_{\rm rms} = u_{\rm rms}$ , where w is the velocity component normal to the laser plane, as

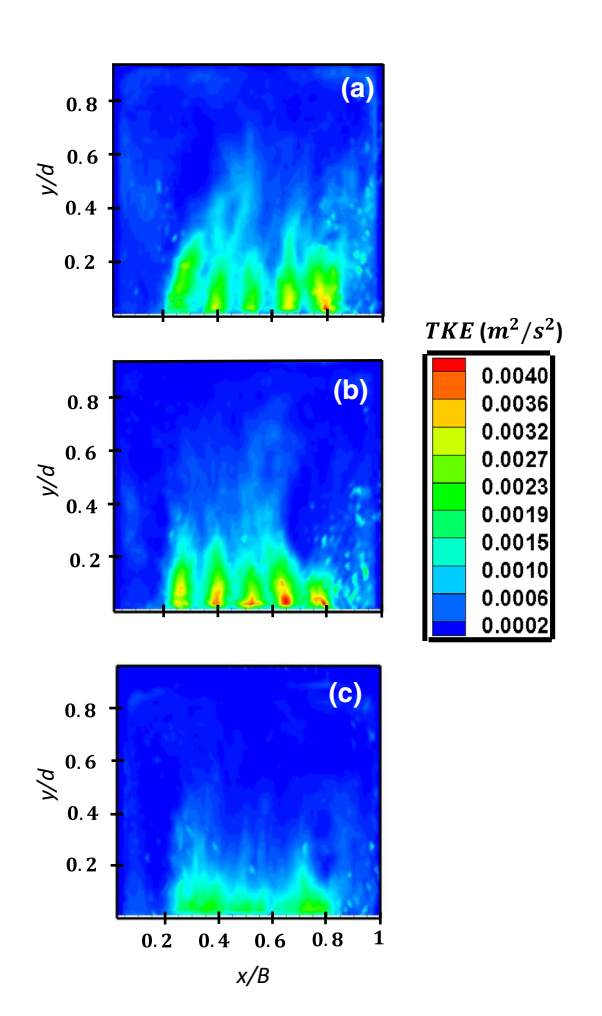


**Fig. 4** TKE contour maps for different combinations of *S* and *f*: **a** S=0.03 m and f=6 Hz for Run 1, **b** S=0.05 m and f=3.5 Hz for Run 2, and **c** S=0.07 m and f=2.5 Hz for Run 3

some others have done; e.g., McKenna and McGillis 2004; McCorquodale and Munro 2017).

The planar distributions of TKE for the three experimental runs are shown in Fig. 4. Turbulence generated by grid oscillation has a maximum value close to the grid, and it decays with increasing distance from the grid. This spatial decay of turbulence is qualitatively consistent with previous studies (Thompson and Turner 1975; Hopfinger and Toly 1976; Atkinson et al. 1987; De Silva and Fernando 1994; Matsunaga et al. 1999; Bennett et al. 2014), but as shown below, decay rates vary due to the presence of secondary circulation. The planar distribution of TKE is similar for Runs 1 and 2, but it is different for Run 3. In Runs 1 and 2 with S/M less than and equal to 1, TKE maxima are observed at the grid nodes, and turbulence diffuses to a distance v/d $\approx 0.4$  before decreasing with height above the grid. In Run 3, with the largest value of S and S/M greater than 1, TKE maxima are not clearly observable at the grid nodes and TKE is relatively smaller at y/d > 0.4 with the same scaling employed in Runs 1 and 2.

#### 3.2 Mean flow

The mean kinetic energy MKE per unit mass at a point, due to the presence of the secondary flow, is defined by

$$MKE = 0.5([u]^2 + [v]^2)$$
(11)

Horizontally averaged values (indicated by angled brackets) of MKE and TKE are calculated to explore their variation in the vertical direction and are defined as

$$\langle MKE \rangle = \frac{1}{B} \int_{x=0}^{B} MKE dx$$
 (12)

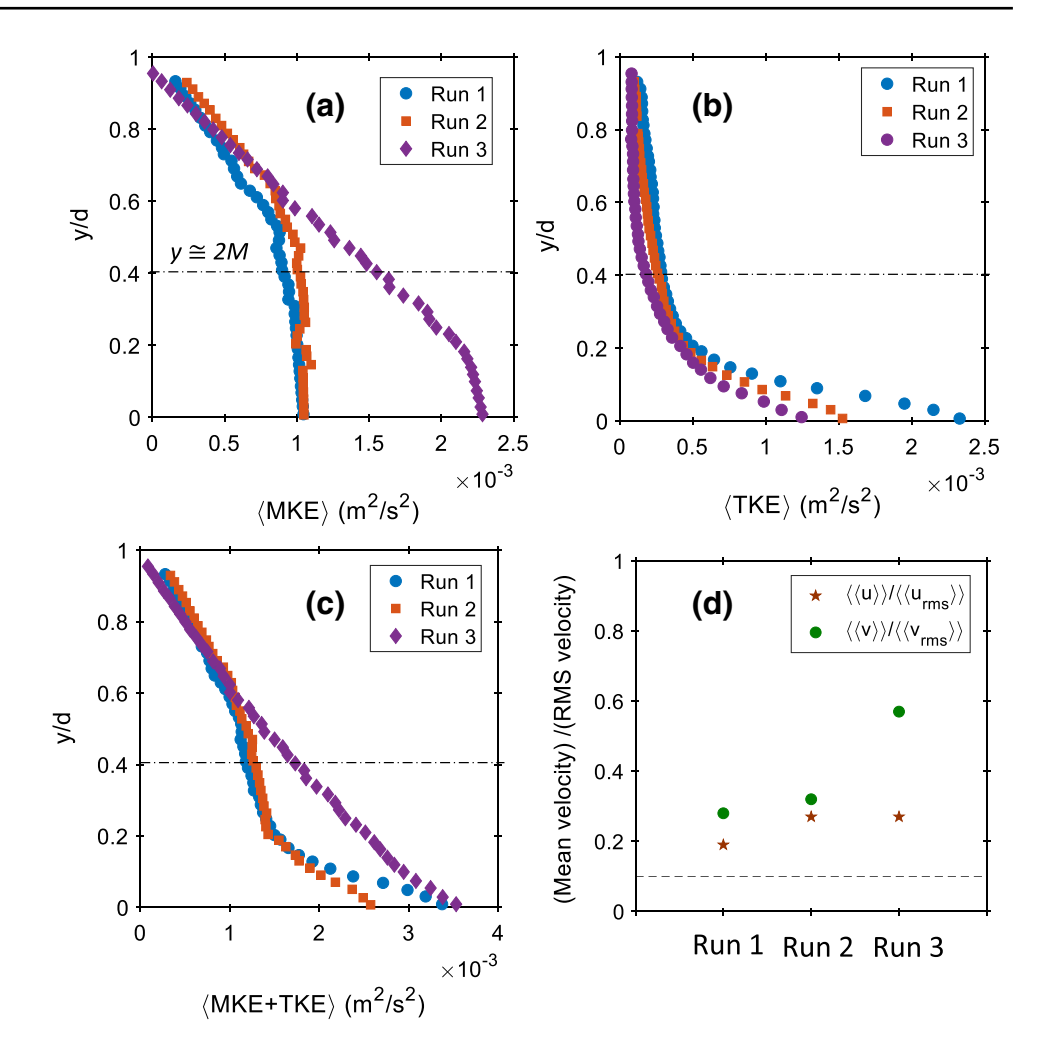
$$\langle \text{TKE} \rangle = \frac{1}{B} \int_{-\infty}^{B} \text{TKE} dx$$
 (13)

Vertical distributions of  $\langle MKE \rangle$  and  $\langle TKE \rangle$  are plotted in Fig. 5 as functions of normalized height above the grid y/d. Figure 5a shows that  $\langle MKE \rangle$  is almost unchanged in the region close to the grid for Runs 1 and 2 (i.e.,  $y/d < 0.4 \cong 2$  M, which is shown using a horizontal dashed line in Figs. 5a, b), and it then decreases nearly linearly toward the water surface. For y/d < 0.4,  $\langle MKE \rangle$  values for Run 3 are more than two times larger than those for Runs 1 and 2, and the linear decrease starts at a lower height, at  $y/d \cong 0.2$ .

The differences between  $\langle MKE \rangle$  values for Runs 2 and 3 are much greater than the differences between values for Runs 1 and 2, while the step change in S is the same



Fig. 5 Vertical profiles of horizontally-averaged  $\mathbf{a}$  mean kinetic energy,  $\mathbf{b}$  turbulent kinetic energy,  $\mathbf{c}$  total kinetic energy, and  $\mathbf{d}$  the ratio of spatially-averaged mean velocity to the spatially-averaged turbulent velocity. The horizontal dashed line in parts  $\mathbf{a}$ ,  $\mathbf{b}$  and  $\mathbf{c}$  shows y/d=2 M. Below this line is the region close to the grid. The horizontal dashed line in (d) shows the criterion for neglecting mean velocity produced in OGTs



( $\pm 0.02$  m). This result suggests that the ratio S/M plays an important role in formation of secondary circulations with substantial mean kinetic energy, as previously noted. In Runs 1 and 2, S/M is less than or equal to 1, respectively, but S/M = 1.4 in Run 3 (Table 1).

Values of  $\langle TKE \rangle$  increase as S decreases, especially in the region close to the grid (y/d < 0.2) which is dissimilar to  $\langle MKE \rangle$  (Fig. 5b). The vertical profiles of total kinetic energy per unit mass, defined as the sum of  $\langle MKE \rangle$  and  $\langle TKE \rangle$ , are shown in Fig. 5c. Larger values of total kinetic energy in Run 3 for y/d < 0.6 are mostly due to the higher  $\langle MKE \rangle$  values, again associated with S/M > 1. The kinetic energy of the secondary flow accounts for nearly 60% of total kinetic energy in Run 3.

Ratios of the spatially or volumetrically averaged mean velocity to the spatially averaged turbulent velocity for each velocity component can be calculated by vertically integrating the horizontally averaged values (denoted with double angled brackets). In all runs, the ratio for the vertical velocity component is greater than the horizontal component (Fig. 5d). In other words, the mean flow relative to the turbulence in the vertical direction is stronger than the mean flow in the

horizontal direction. This figure also shows that larger values of *S* produce stronger mean flow velocities, especially in the vertical direction. Here, the vertical component of mean flow for all runs is stronger than 20% of the vertical turbulent velocities, and in Run 3 with the largest *S*, this percentage is as high as 60% (Fig. 5d). This result again suggests that *S* and *S/M* have a measurable impact on the strength of secondary circulation, especially in the vertical direction.

# 3.3 Turbulence characteristics

The impacts of secondary circulation on turbulence are examined by analyzing distributions of turbulent velocities and turbulent integral length scales over the flow depth. Figures 6a and b show the variations of horizontal and vertical turbulent velocities normalized by fS, with flow depth normalized by  $\sqrt{MS}$ . These normalizations are chosen to be consistent with Hopfinger and Toly (1976), who found

$$\frac{u_{\rm rms}}{fS} = c_4 \frac{\sqrt{MS}}{y} \tag{14a}$$



Experiments in Fluids (2020) 61:225 Page 9 of 13 225

$$\frac{v_{\rm rms}}{fS} = c_5 \frac{\sqrt{MS}}{y} \tag{14b}$$

where  $c_4$  and  $c_5$  are constants. Figure 6 indicates that the horizontally-averaged turbulent velocities decay toward the water surface in agreement with previously reported trends. This figure also includes data from Hopfinger and Toly (1976) using S/M = 0.8, Fernando and De Silva (1993) using S/M = 0.44 and 0.18, and Cheng and Law (2001) using S/M = 0.8, as well as Eq. (14) for fitted values for  $c_4$  and  $c_5$ . Using Eq. 14,  $c_4 = 0.1$  provides the best fit to horizontal velocity data close to the grid, while  $c_4 = 0.15$  provides the best fit in the central flow region (i.e., the region far from the grid and water surface; Fig. 6a). Although the overall trend on Eq. 14 agrees with observations, there is no single coefficient that best captures the experimental variability in the vertical component (Fig. 6b).

For the previous studies shown in Fig. 6, $\langle u_{\rm rms} \rangle$  was measured and  $\langle u_{\rm rms} \rangle = \langle v_{\rm rms} \rangle$  by assuming isotropic turbulence. In practice, turbulence is not completely isotropic (McDougall 1979; De Silva and Fernando 1994). Normalized  $\langle u_{\rm rms} \rangle$  data for the present experiments collapse onto a single curve (Fig. 6a), implying fS is the appropriate scaling parameter. Yet the normalized  $\langle v_{\rm rms} \rangle$  plots do not collapse onto a single curve (Fig. 6b). This suggests that the vertical turbulent velocity is influenced by the stroke size S and the effects of secondary circulation, particularly the presence of considerable mean flow in the vertical direction (Fig. 5d).

Horizontal  $\zeta_x$  and vertical  $\zeta_y$  integral length scales are calculated using a spatial auto-correlation (Pope 2000),

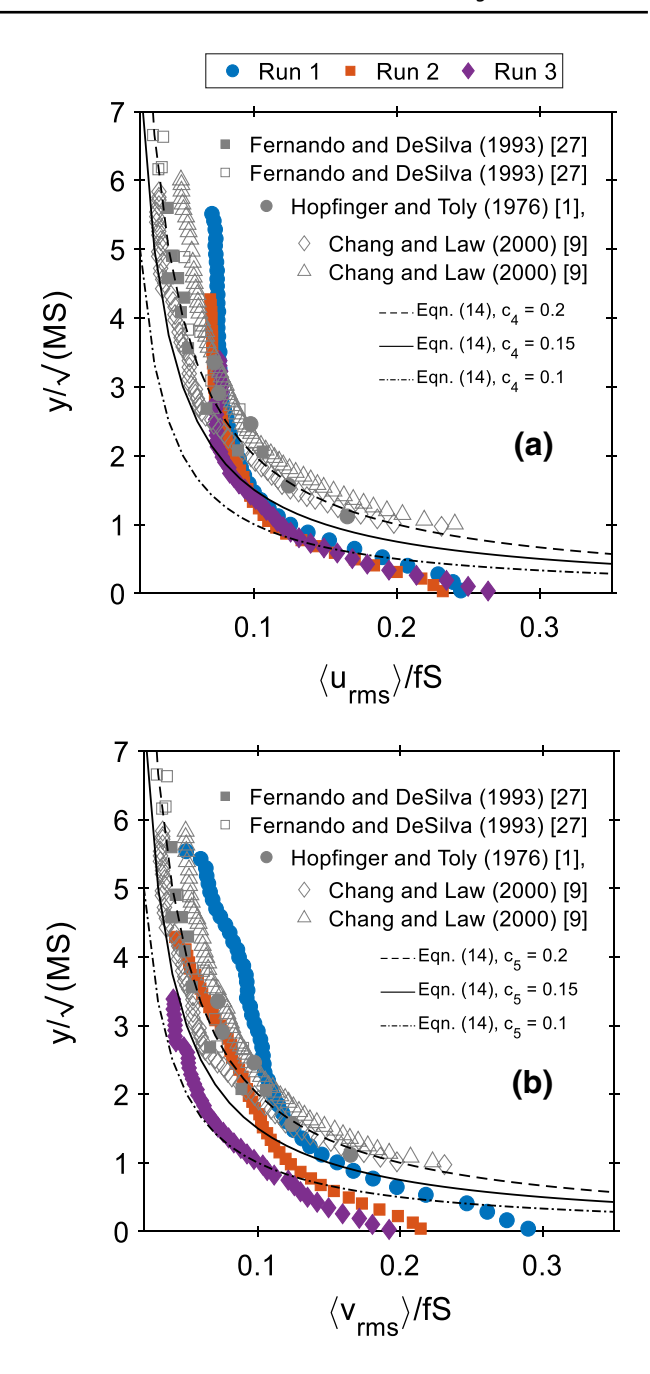


Fig. 6 Vertical profiles of horizontally-averaged **a** horizontal turbulent velocity, and **b** vertical turbulent velocity

$$R_{xx}(\chi, x, y) = [u'(x, y, t)u'(x + \chi, y, t)]; \quad R_{yy}(\chi, x, y) = [v'(x, y, t)v'(x, y + \chi, t)]$$
(15)

$$\zeta_{x}(x,y) = \frac{1}{R_{xx}(0,x,y)} \int_{0}^{\chi_{0}} R_{xx}(\chi,x,y) d\chi; \quad \zeta_{y}(x,y) = \frac{1}{R_{yy}(0,x,y)} \int_{0}^{\chi_{0}} R_{yy}(\chi,x,y) d\chi$$
 (16)



225 Page 10 of 13 Experiments in Fluids (2020) 61:225

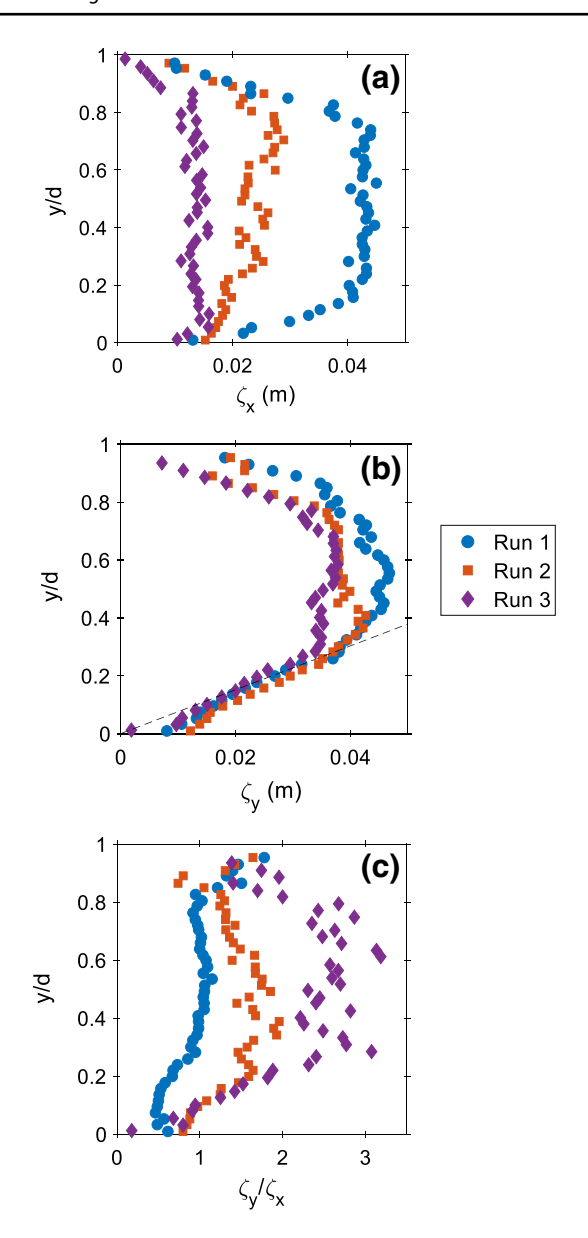
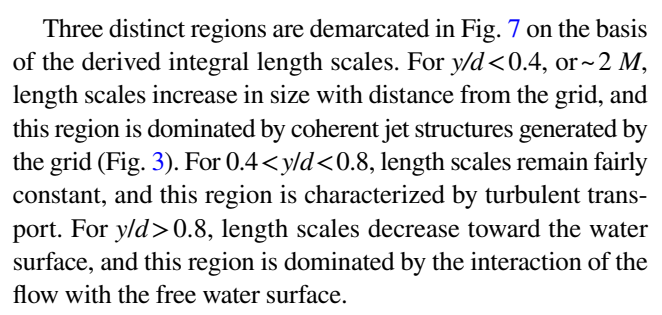


Fig. 7 Vertical profiles of horizontally-averaged  $\bf a$  horizontal integral length scale and  $\bf b$  vertical integral length scale, and  $\bf c$  their ratio. The dashed line in  $\bf b$  shows a linear fit to experimental data in the region close to the grid, y/d < 0.4

where  $\chi$  is the spatial lag and  $\chi_0$  is the spatial lag at which the correlation function first becomes zero. Horizontally averaged integral length scales are shown in Fig. 7. For Run 1,  $\zeta_x$  increases from about 0.02 m near the grid to a maximum of about 0.04 m at y/d=0.2. This length scale remains almost unchanged to y/d=0.8, and it then decreases toward the water surface. For Runs 2 and 3,  $\zeta_x$  is almost constant over depth, with a value of about 0.02 m. In all combinations of S and f,  $\zeta_y$  increases from about 0.01 m near the grid to a maximum values of 0.048, 0.041, and 0.032 for Runs 1, 2, and 3, respectively, at  $y/d \approx 0.5$ . Above this height, the vertical length scales decrease toward the water surface.



Previous studies suggested that the turbulent integral length scale is linearly proportional to the vertical distance from the source of turbulence (Eq. 3). Since turbulence in the OGT is ideally isotropic, the horizontal integral length scale should be nearly equal to the vertical integral length scale (Thompson and Turner 1975; Hopfinger and Toly 1976; De Silva and Fernando 1998; Matsunaga et al. 1999), or

$$\zeta_x \cong \zeta_y = \zeta \tag{17}$$

The value of  $c_3$  in Eq. 3 depends on M and S if S/M < 0.8, but it depends only on M when S/M > 0.8 (Hopfinger and Toly 1976). For all experiments reported here, the linear proportionality between integral length scales and depth with  $c_3 = 0.7$  approximately describes  $\zeta_y$  in the region close to the grid (y/d < 0.4), but it does not hold for greater distances away from the grid (Fig. 7b). Moreover, no linear relationship is observed for  $\zeta_y$  (Fig. 7a).

The integral length scales  $\zeta_x$  and  $\zeta_y$  are not equal, and therefore turbulence is not isotropic. The ratio  $\zeta_y/\zeta_x$ , a measure of the degree of anisotropy, is almost 1 for Run 1, between 1 and 2 for Run 2, and greater than 2 for Run 3 (Fig. 7c). This suggests that for S/M < 1, turbulent eddies are roughly circular in shape. But for  $S/M \ge 1$ , the turbulent eddies are elongated vertically, and as S and S/M become larger,  $\langle \zeta_y \rangle / \langle \zeta_x \rangle$  also increases.

# 4 Discussion

The experimental results show that oscillating grid turbulence in a mixing box can be associated with significant secondary circulation. The grid movement conditions determined by the combination of f and S affect the intensity of these large-scale motions, but the general pattern is the same for all combinations tested here. The strength of secondary circulation is directly dependent on S; as S becomes larger, the magnitude of mean velocities increases and the contribution of secondary circulations to total kinetic energy becomes larger. The secondary circulation patterns affect turbulent transport and mixing. In an ideal zero-mean-shear flow, turbulent transport occurs by pressure fluctuations and turbulent shear stresses. Yet in the presence of secondary



Experiments in Fluids (2020) 61:225 Page 11 of 13 225

flow, turbulent transport also occurs by the advection of the mean flow. In both cases, with and without mean flow, TKE decays vertically. In addition to greater secondary flow and transport with larger *S*, the present results indicate that turbulence is not completely isotropic.

Similar to McCorquodale and Munro (2017), who used the Reynolds stress transport equation to analyze the interaction of turbulence generated by an oscillating grid and a solid boundary aligned parallel to the grid and positioned below and far from the grid, we consider the impact of secondary circulation using the turbulent kinetic energy equation. The steady state form of this equation can be written as

$$[v]\frac{d(\text{TKE})}{dy} = -\frac{d}{dy}\left(\frac{[v'p']}{\rho_0} + [\text{TKE}v']\right) - [u'v']\frac{\partial[u]}{\partial y} - \varepsilon$$
(18)

where  $\rho_0$  is water density, p' is pressure fluctuations, and  $\varepsilon$  is the dissipation of TKE per unit of mass. Turbulent velocity scale can be written as  $(TKE)^{1/2}$ , and the dissipation term can be written as  $\varepsilon = A_1(TKE^{3/2}/\zeta)$ , where  $A_1$  is a constant (Rubin and Atkinson 2001). Based on the Bernoulli equation and neglecting significant head differences, pressure fluctuations are proportional to velocity squared and the pressure fluctuation term can be scaled by  $TKE^{3/2}$ . The vertical flux of TKE also can be scaled by  $TKE^{3/2}$ .

The assumption  $u' \sim bv'$ , where b is a constant, serves as a reasonable approximation for parameterization of the TKE equation. The shear production term can be scaled by  $(bv_{\rm rms}^2)\frac{\partial [u]}{\partial y}$  or  $({\rm TKE})\frac{\partial [u]}{\partial y}$ . Substituting the parameterized versions of each term into Eq. 18 yields

$$A_4[v] \frac{d(\text{TKE})}{dy} = -\frac{d}{dy} \left( A_3 \text{TKE}^{3/2} \right) - A_2 \text{TKE} \frac{\partial [u]}{\partial y} - A_1 \left( \frac{\text{TKE}^{3/2}}{\zeta} \right)$$
(19)

where  $A_2$ ,  $A_3$  and  $A_4$  are constants.

In the absence of mean flow (i.e., secondary circulation), the left-hand side and the second term on the right-hand side of Eq. 19 are equal to zero, and

$$A_3 \frac{d\left(\text{TKE}^{3/2}\right)}{dy} = -A_1 \left(\frac{\text{TKE}^{3/2}}{\zeta}\right) \tag{20}$$

Equation 19 indicates that in the presence of measurable secondary circulation associated with mean flow, the vertical distribution of TKE is controlled by five terms, (1) advective transport flux, (2) shear production, (3) pressure fluctuation, (4) vertical turbulent transport flux and (5) dissipation. However, in the absence of mean flow, Eq. 20 indicates vertical distribution of TKE is controlled by only three terms, pressure fluctuation, vertical turbulent transport flux, and dissipation. Effects of two mean-flow dependent terms, advective transport flux and shear production, on vertical

TKE distribution is demonstrated by experimental results. For example, in the region close to the grid, y/d < 0.4, there is a strong mean flow due to secondary circulation (Figs. 3, 5a) and Eq. 19 governs vertical TKE transport, TKE decays quickly (Figs. 4a, b, 5b) and the vertical integral length scale increases with height (Fig. 7b). In the region far from the grid, 0.4 < y/d < 0.8, the mean flow velocity associated with the secondary circulation is smaller (Figs. 3, 5a) and Eq. 20 governs vertical TKE transport, TKE decays slowly (Figs. 4a, b, 5b) and the vertical integral length scale (Fig. 7b) remain almost unchanged with height above the grid. Finally, in the region close to the water surface, y/d > 0.8, neither Eq. 19 or 20 governs vertical distribution of TKE due to the presence of the free surface and the interactions between fluid and gas phases leading to the vertical integral length scale decreasing toward zero (Fig. 7b).

In the present experiments, a correct-end condition grid with 30% solidity is used in a box with D/B < 1, f < 7 Hz, and S > 0.01 m, thus satisfying previously reported criteria to avoid secondary flows. For Runs 1, 2, and 3, S/M = 0.6, 1, and 1.4, respectively. Using the  $S/M \le 1$  criterion reported by Hopfinger and Toly (1976) and McDougall (1979), significant secondary flow should have been observed only in Run 3. Yet non-negligible secondary circulations (i.e., greater than 20% contribution to total kinetic energy) are observed in all runs. Thus the criterion S < M is insufficient to guarantee the absence of secondary circulation. In addition, as the stroke length increases and S/M becomes increasingly greater than 1, the mean flow associated with large circulation motions increases.

While the formation of secondary circulation associated with oscillating-grid turbulence has been previously observed (Fernando and De Silva 1993; Dohan and Sutherland 2002; McKenna and McGillis 2004; Bennett et al. 2014), the effect of grid oscillation conditions on the strength of these large-scale motions has not been reported. Empirical evidence presented here supports the conclusion that S affects the strength of secondary circulation patterns independent of Re<sub>G</sub>. In most previous work with OGTs, the grid was located near the water surface, and the bottom floor was at the maximum distance from the source of turbulence. Huppert et al. (1995) were the first to use a mixing box with the grid near the bottom to study particle suspension. The location of the grid at the bottom and the interaction of gridgenerated jets with the solid floor of the box might affect the formation of large circulation motions or alter the intensity of the mean flow. To further examine these effects, experiments should be conducted with the same combinations of S and f in a mixing box with the grid located at different distances from the bottom.

Finally, all data in the present tests were collected in a single plane at  $z/B \approx 0.25$ . The flow field exhibits spatial variations of time-mean flow and turbulent flow as a function of



225 Page 12 of 13 Experiments in Fluids (2020) 61:225

distance from the box wall (Orlins and Gulliver 2003). The magnitudes of secondary circulation and turbulent kinetic energy observed herein may depend on the location of the measurements. Additional experiments with different oscillation grid conditions for all planes within the box would be required to document changes to the three-dimensional flow field.

Moreover, the results presented for each run were averaged over five tests with average relative standard error atapoint of 9%, 18% and 8% for u, v and TKE, respectively. This result is consistent with McKenna and McGillis (2004), who also observed variability in results of different experimental runs with nominally identical test conditions. The observed variability among repetitions of a given test do not, however, explain the differences between tests. In addition, the data were tested and shown to be consistent with a steady state condition.

# **5 Conclusions**

The effects of the grid oscillation conditions on the formation and the strength of secondary circulation in a mixing box were investigated. The grid shape and solidity, the number of grid bars and their dimensions, the mesh spacing, and the distance between the measured flow field and the sidewall of the tank were held constant, while three different combinations of the stroke length and the oscillation frequency were examined. These combinations were chosen to maintain an approximately constant grid Reynolds number. Two-dimensional PIV data were collected at 80 Hz and time-averaged, and turbulent signatures of the flow field were calculated.

The primary results from this experimental campaign are summarized as follows:

- Two symmetric secondary circulation patterns were generated in all runs. The general patterns of these secondary flows were similar but the intensities were different.
- 2. The magnitude of secondary flow within the mixing box contributed a minimum of 20% of the total kinetic energy of the generated motion, and the mean kinetic energy of the secondary circulation accounted for a larger fraction of the total kinetic energy of the fluid motion, relative to turbulent kinetic energy, than has been previously reported. As *S* increased and *S/M* became increasingly greater than 1, the mean flow magnitude, especially in the vertical direction, became stronger.
- Integral length scales for turbulence were not equal in horizontal and vertical directions, and turbulent flow was not isotropic in the presence of secondary circu-

- lation. The linear relationship between integral length scale and depth previously reported was found to hold only for the vertical integral length scale in the region close to the grid (y < 2 M).
- 4. Flow characteristics in the vertical direction are divided into three distinct regions: (i) for  $y/d < 0.4 \cong 2 M$ , this region is characterized by maxima for mean flow, TKE, and TKE decay rate, (ii) for 0.4 < y/d < 0.8, this region is characterized by turbulent transport with slow TKE decay rate and nearly constant vertical integral length scales, and (iii) for 0.8 < y/d, flow characteristics are dominated by the interaction of the flow with the free water surface.

A box with an oscillating grid can be used to examine fluid mixing across a density interface, interfacial gas exchange, the physics of turbulence, and turbulent transport and sediment suspension mechanics in geophysical flows. The results presented here suggest that secondary flow is associated with oscillating grid and it influences the spatial turbulence decay law previously derived for OGTs. It should be noted that in these experiments, the grid location was close to the solid bottom boundary of the box, and the interaction of random jets with the solid boundary might affect the formation of secondary circulation.

## References

- Atkinson JF, Damiani L, Harleman DRF (1987) A comparison of velocity measurements using a laser anemometer and a hot-film probe, with application to grid-stirring entrainment experiments. Phys Fluid 10:3290–3292
- Belinsky M, Rubin H, Agnon Y (2005) Characteristics of resuspension, settling and diffusion of particulate matter in a water column. Environ Fluid Mech 5:415–441. https://doi.org/10.1007/s1065 2-004-7302-3
- Bennett SJ, Atkinson JF, Hou Y (2013) Turbulence modulation by suspended sediment in a zero mean-shear geophysical flow. In: Venditti JG, Best J, Church M, Hardy RJ (eds) Coherent flow structures at the earth's surface. Wiley, Chichester, pp 309–321. https://doi.org/10.1002/9781118527221.ch20
- Bennett SJ, Best JL (1995) Particle size and velocity discrimination in a sediment-laden turbulent flow using phase Doppler anemometry. J Fluids Eng 117:505. https://doi.org/10.1115/1.2817291
- Bennett SJ, Hou Y, Atkinson JF (2014) Turbulence suppression by suspended sediment within a geophysical flow. Environ Fluid Mech 14:771–794. https://doi.org/10.1007/s10652-013-9323-2
- Cheng NS, Law AW (2001) Measurments of turbulence generated by oscillating grid. Hydraul Eng 127:201–208
- De Silva IPD, Fernando HJS (1994) Oscillating grids as a source of nearly isotropic turbulence. Phys Fluids 6:2455–2464. https://doi.org/10.1063/1.868193
- De Silva IPD, Fernando HJS (1998) Experiments on collapsing turbulent regions in stratified fluids. J Fluid Mech 358:29–60. https://doi.org/10.1017/S0022112097008094
- Dohan K, Sutherland BR (2002) Turbulence time scales in mixing box experiments. Exp Fluids 33:709–719. https://doi.org/10.1007/s00348-002-0536-2



Experiments in Fluids (2020) 61:225 Page 13 of 13 225

Drayton MJ (1993) Eularian and lagrangian studies of inhomogeneous turbulence generated by an oscillating grid. Ph.D. thesis, King's College, University of Cambridge

- Fernando HJS, De Silva IPD (1993) Note on secondary flows in oscillating-grid, mixing-box experiments. Phys Fluids 5:1849–1851. https://doi.org/10.1063/1.858808
- Guadayol O, Peters F, Stiansen JE (2009) Evaluation of oscillating grids and orbital shakers as means to generate isotropic and homogeneous small-scale turbulence in laboratory enclosures commonly used in plankton studies. Limnol Oceanogr Methods 7:287–303, https://doi.org/10.4319/lom.2009.7.287
- Hannoun IA, Fernando HJS, List EJ (1988) Turbulence structure near a sharp density interface. J Fluid Mech 189:189–209. https://doi. org/10.1017/S0022112088000965
- Herlina JGH (2008) Experiments on gas transfer at the air-water interface induced by oscillating grid turbulence. J Fluid Mech 594:183–208. https://doi.org/10.1017/S0022112007008968
- Hopfinger EJ, Toly JA (1976) Spatially decaying turbulence and its relation to mixing across density interfaces. J Fluid Mech 78:155–175. https://doi.org/10.1017/S0022112076002371
- Huppert HE, Turner JS, Hallworth MA (1995) Sedimentation and entrainment in dense layers of suspended particles stirred by an oscillating grid. J Fluid Mech 289:263. https://doi.org/10.1017/ S0022112095001339
- Janzen JG, De Souza LBS, Schulz HE (2003) Kinetic energy in grid turbulence: comparison between data and theory. J Brazil Soc Mech Sci Eng 25:347–351. https://doi.org/10.1590/S1678-58782 003000400006
- Lacassagne T, Lyon A, Simoëns S, El Hajem M, Champagne JY (2020) Flow around an oscillating grid in water and shear-thining polymer solution at low Reynolds number. Exp Fluids 61:15
- Liu AC, Huhe A, Taoi L (2011) Sediment incipience in turbulence generated in a square tank by a vertically oscillating grid. JSTOR 39:465–468
- Matinpour H, Bennett SJ, Atkinson JF (2015) Investigation Turbulent Flow Charcateristics using Mixing Box. 46th Annual Binghamton Geomorphology Symposium, Spemtember 2015, Buffalo, NY USA
- Matinpour H, Bennett SJ, Atkinson JF, Guala M (2019) Modulation of time-mean and turbulent flow by suspended sediment. Phys Rev Fluids. https://doi.org/10.1103/PhysRevFluids.4.074605
- Matsunaga N, Sugihara Y, Komatsu T, Masuda A (1999) Quantitative properties of oscillating-grid turbulence in a homogeneous fluid. Fluid Dyn Res 25:147–165
- McCorquodale MW, Munro RJ (2017) Experimental study of oscillating-grid turbulence interacting with a solid boundary. J Fluid Mech 813:768–798. https://doi.org/10.1017/jfm.2016.843
- McCorquodale MW, Munro RJ (2018) A method for reducing mean flow in oscillating-grid turbulence. Exp Fluids 59:1–16. https://doi.org/10.1007/s00348-018-2636-7
- McDougall TJ (1979) Measurments of turbulence in a zero-mean-shear mixed layer. J Fluid Mech 94(03):409–431

- McGrath JL, Fernando HJS, Hunt JCR (1997) Turbulence, waves and mixing at shear-free density interfaces. Part 2. Laboratory experiments. J Fluid Mech 347:235–261. https://doi.org/10.1017/S0022
- McKenna SP, McGillis WR (2004) Observations of flow repeatability and secondary circulation in an oscillating grid-stirred tank. Phys Fluids 16:3499–3502. https://doi.org/10.1063/1.1779671
- Medina P, Sánchez MA, Redondo JM (2001) Grid stirred turbulence: applications to the initiation of sediment motion and lift-off studies. Phys Chem Earth, Part B Hydrol Ocean Atmos 26:299–304. https://doi.org/10.1016/S1464-1909(01)00010-7
- Mohtar WHM (2016) Oscillating-grid turbulence at large strokes: revisiting the equation of Hopfinger and Toly. J Hydrodyn 28:473–481. https://doi.org/10.1016/S1001-6058(16)60651-0
- Orlins JJ, Gulliver JS (2003) Turbulence quantification and sediment resuspension in an oscillating grid chamber. Exp Fluids 34:662–677. https://doi.org/10.1007/s00348-003-0595-z
- Pope SB (2000) Turbulent flow. Cambridge University Press, Cambridge
- Pujol D, Colomer J, Serra T, Casamitjana X (2012) A model for the effect of submerged aquatic vegetation on turbulence induced by an oscillating grid. Estuar Coast Shelf Sci 114:23–30. https://doi. org/10.1016/j.ecss.2011.08.020
- Rastello M, Michallet H, Marié JL (2020) Sediment erosion in zeromean-shear turbulence Sediment erosion in zero-mean-shear turbulence. Phys Fluids. https://doi.org/10.1063/1.5141943
- Redondo JM, De Madron XD, Medina P (2001) Comparison of sediment resuspension measurements in sheared and zero-mean turbulent flows. Cont Shelf Res 21:2095–2103. https://doi.org/10.1016/S0278-4343(01)00044-9
- Rubin H, Atkinson JF (2001) Environmental fluid mechanics. CRC Press, Boca Raton
- Schulz HE, Janzen JG, Souza KCDO (2006) Experiments and theory for two grids turbulence. J Brazil Soc Mech Sci Eng 28:216–223. https://doi.org/10.1590/S1678-58782006000200011
- Thompson SM, Turner JS (1975) Mixing across an interface due to turbulence generated by an oscillating grid. J Fluid Mech 67:349–368. https://doi.org/10.1017/S0022112075000341
- Variano EA, Cowen EA (2008) A random-jet-stirred turbulence tank. J Fluid Mech 604:1–32. https://doi.org/10.1017/S0022112008000645
- Villermaux E, Sixou B, Gagne Y (1995) Intense vortical structures in grid-generated turbulence. Phys Fluids 7:2008–2013. https://doi.org/10.1063/1.868512

**Publisher's Note** Springer Nature remains neutral with regard to jurisdictional claims in published maps and institutional affiliations.

